

DISCOVERY OF ROTATIONAL MODULATIONS IN THE PLANETARY-MASS COMPANION 2M1207B: A SLOW ROTATION PERIOD AND HETEROGENEOUS CLOUDS IN A LOW GRAVITY ATMOSPHERE

YIFAN ZHOU¹, DÁNIEL APAI^{1,2,3}, GLENN SCHNEIDER¹, MARK S. MARLEY⁴

Draft version September 23, 2015

ABSTRACT

Rotational modulations of brown dwarfs have recently provided powerful constraints on the properties of ultra-cool atmospheres, including longitudinal and vertical cloud structures and cloud evolution. Furthermore, periodic light curve directly probes the rotational periods of ultra-cool objects.

We present here, for the first time, time-resolved high-precision photometric measurements of a planetary-mass companion, 2MASS1207b, to a brown dwarf primary. We observed the binary system with HST/WFC3 in two bands and with two spacecraft roll angles. Using point spread function-based photometry we reach a nearly photon-noise limited photometric accuracy for both components. While the primary is consistent with a flat lightcurve, the secondary shows modulations that are clearly detected in the combined lightcurve as well as in different subsets of the data. The amplitudes are 1.45% in the F125W and 0.92% in the F160W filters; we find a consistent period of $10.2^{+0.9}_{-0.8}$ h and similar phase in both bands. The J- and H-band amplitude ratio of 2M1207 bis very similar to a field brown dwarf that has identical spectral type but different J-H color. Importantly, our study also measures, for the first time, the rotational period for directly an imaged planetary-mass companion.

Subject headings: brown dwarfs – planets and satellites: atmospheres – planets and satellites: individual (2M1207 b) – techniques: photometric

1. INTRODUCTION

Presence of condensate clouds is one the most unique features of the ultra-cool atmosphere of directly imaged exoplanet and brown dwarfs. Studies of formation and properties of condensate clouds (e.g. [Ackerman & Marley 2001](#); [Burrows et al. 2006](#); [Helling et al. 2008](#); [Allard et al. 2012](#)) have achieved great improvement in understanding the cloud behavior across different spectral types, especially in the explanation of L-T transition (e.g. [Burrows et al. 2006](#); [Marley et al. 2010](#)). Surface gravity is suggested to be the second key parameters in defining cloud structures (e.g. [Marley et al. 2012](#)) after effective temperature. Low surface gravity objects (e.g. HR8799 bcd, [Marois et al. \(2008\)](#), 2M1207 b, [Chauvin et al. \(2004\)](#)) are significantly redder and under-luminous compared to brown dwarfs. The anomalous color and luminosity of low surface gravity objects supports model including unusually thick clouds ([Currie et al. 2011](#); [Madhusudhan et al. 2011](#); [Skemer et al. 2011, 2012](#)). However, due to lack of observational constraint, the dependence of cloud properties on surface gravity is not very well modeled.

Intensity modulations introduced by heterogeneous clouds can be directly observed and studied via time resolved observation and rotational mapping. These techniques isolate the effect of cloud properties and obtained great success in determining the rotation period and unveiling the structures of the atmosphere of brown dwarfs (e.g. [Apai et al. 2013](#); [Buenzli et al. 2012, 2015](#); [Bur-](#)

[gasser et al. 2013](#); [Radigan et al. 2012](#); [Yang et al. 2014](#); [Metchev et al. 2015](#); [Heinze et al. 2015](#)). [Kostov & Apai \(2013\)](#) demonstrated that these techniques can be applied to directly imaged exoplanets, too, allowing comparative studies of objects with different surface gravities. However, high contrast magnifies the challenges for directly imaged exoplanets and planetary-mass companions to acquire high-precision light curves comparing to brown dwarfs.

2M1207 b [Chauvin et al. \(2004\)](#) is the first directly imaged planetary-mass companion. [Chauvin et al. \(2005\)](#); [Song et al. \(2006\)](#) confirmed that 2M1207 b and its host 2M1207 A form a bound, co-moving system. 2M1207 A and b have an angular separation of $0.78''$, which is corresponding to a projected separation of 41.2 AU at a distance of 52.4 pc (e.g. [Ducourant et al. 2008](#)). Combining 2M1207 b's age and near infrared luminosity with brown dwarf cooling models (e.g. [Baraffe et al. 2003](#)), the object's mass is estimated to be 2.3-4.8 M_{Jup} ([Barman et al. 2011](#)). Even though a circumsubstellar disk was discovered around 2M1207A ([Sterzik et al. 2004](#)), the high companion-to-host mass ratio and large separation argue for binary-like gravitational fragmentation formation ([Mohanty et al. 2007](#)).

Early observations revealed that 2M1207 b's color is much redder and its near-infrared luminosity is much lower than those of field brown dwarfs with similar spectra (e.g. [Mohanty et al. 2007](#); [Skemer et al. 2011](#); [Barman et al. 2011](#)). 2M1207b's luminosity – as derived from near-infrared photometry – is ~ 2.5 mag lower than that predicted based on its mid- to late L spectral type and effective temperature of ~ 1600 ([Patience et al. 2010](#)). Based multi-band near-infrared photometry [Skemer et al. \(2011\)](#) argued that the apparent under-luminosity of 2M1207 b may be explained by a model of a spatially heterogeneous atmosphere composed of patches

¹ Department of Astronomy/Steward Observatory, The University of Arizona, 933 N. Cherry Ave., Tucson, AZ, 85721, USA, yiifzhou@email.arizona.edu

² Lunar and Planetary Laboratory, The University of Arizona, 1640 E. University Blvd., Tucson, AZ 85718, USA

³ Earths in Other Solar Systems Team, NASA Nexus for Exoplanet System Science

⁴ NASA Ames Research Center, Naval Air Station, Moffett Field, Mountain View, CA 94035, USA

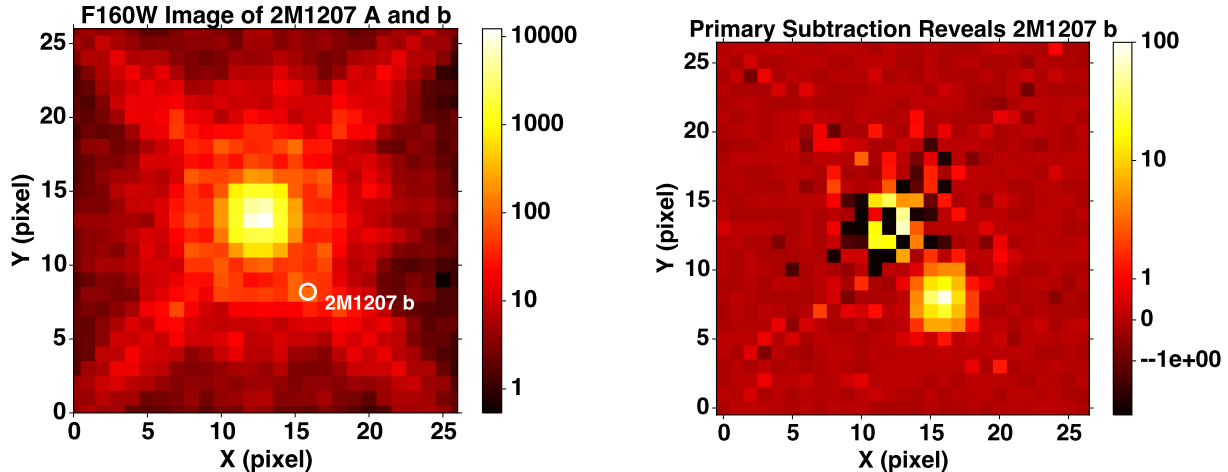


FIG. 1.— Point spread function subtraction allows isolating the secondary and accurately measuring its brightness in our WFC3 F160W images. *Upper*: original image, the position of 2M1207 b is indicated by a white circle. *Lower*: residual image – after the subtraction of the hybrid PSF, 2M1207 b is detected at a high significant level.

of thin and patches of unusually thick clouds. Similarly, Barman et al. (2011) argued that non-local chemical equilibrium could play an equally important role as thick clouds in defining 2M1207b’s color and luminosity.

The discovery of additional planetary-mass companions with similarly red colors and apparent under-luminosity have highlighted 2M1207b as a template of low gravity ultra-cool atmospheres but as of now understanding the composition and structure of clouds and their gravity-dependence remained elusive.

In this *Letter* we present the first, high-cadence, high-precision, time-resolved *Hubble Space Telescope* (HST) photometric time series of 2M1207 b, a directly imaged planetary-mass object. We successfully detect rotational modulation and measure the amplitudes in two bands and determine the rotational period. These observations probe the spatial heterogeneity and vertical structure of clouds in planetary mass objects for the first time.

2. OBSERVATION

We obtained direct images of the 2M1207A+b system on UT 2014 April 11 from 08:07:47 to 16:53:18 using HST and its Wide Field Camera 3 (WFC3, pixel scale=0.130mas/pixel, MacKenty et al. 2008) in the frame of the HST Program GO-13418 (PI: D. Apai). We acquired the observations in filters F125W ($\lambda_{\text{pivot}} = 1245.9$ nm, full width at half maximum (FWHM) = 301.5 nm) and F160W ($\lambda_{\text{pivot}} = 1540.52$, FWHM = 287.9 nm), roughly corresponding to the J and H bands. We used the 256×256 pixels sub-array mode to avoid memory dumps during the observations. In order to provide a near-continuous coverage for detecting modulations we observed the 2M1207 system in 6 consecutive HST orbits, obtaining data with cadence of ~ 1.5 minutes over a baseline of 8 hours and 40 minutes. The observations were interrupted by 58 minutes long Earth occultations every 94 minutes.

The observations applied space craft rolls each two orbit to allow roll-subtraction of the primary (e.g. Song et al. 2006). The telescope roll angles for orbit 1, 3, and 5, and those for 2, 4, and 6 differ by 25° . At the separation of 2M1207 b, this angle difference corresponds to a displacement of $0.34''$, or 2.75 and 2.30 resolution elements

in F125W and F160W, respectively. In each orbit we took 8 SPARS10 exposure sequence with NSAMP=10, alternating between F160W and F125W filters, with 2–3 identical exposures in each exposure sequence. To improve sampling and reduce the risk that the core of point spread function (PSF) is affected by bad pixels, we applied a 4-point dither pattern with differential “X/Y” offsets of 1.375” in the detector frame, providing optimal non-integral (half pixel) step of 10.5 and 8.5 pixels in F125W and F160W, respectively. In total, we obtained 70 images with 10 non-destructive read-outs in F125W and 64 images in F160W with exposure time of 88.4 s for both filters.

3. DATA REDUCTION

3.1. Photometry

We started the reduction from the `flt` files produced by the WFC3’s `calwfc3` pipeline. We did not opt to use `ima` files that contain all non-destructive read-outs, because they provided less information on 2M1207A, which saturated after the first few samples. The `flt` files are results of basic calibration, including dark current correction, non-linearity correction, flat field correction, as well as up-the-ramp fit on the non-destructive read-outs. Pixels with data quality flags “bad detector pixels”, “unstable response”, and “bad or uncertain flat value” were masked out and excluded from further analysis as suggested by previous transit exoplanet spectroscopic observations (e.g. Berta et al. 2012; Kreidberg et al. 2014).

The major challenge of high contrast observation with WFC3/IR is the fact that the detector is significantly under-sampled. 2M1207 A and b are only separated by ~ 6 pixels or ~ 5 FWHM of the PSF on the detector. When applying roll subtraction, notable artifacts are introduced by image shifting and interpolation. *Tiny Tim* PSF simulator (Krist 1995) offers a solution by providing Nyquist or better sampled PSF, but systematic errors of *Tiny Tim* PSF for WFC3 limits its ability in high precision photometry (Biretta 2014). Building on the large number of PSFs obtained in our program at two different roll angles, we followed a novel, two-step approach that uses a hybrid PSF, which combined the strengths of

the roll subtraction-based and the simulated PSF-based approaches. First, based on our observations we observationally derived correction maps for *Tiny Tim* that accurately described the scattered light component for the primary at the correct location on the detector. Second, we carried out a PSF-photometry using hybrid PSFs composed by *Tiny Tim* PSFs and the correction map by simultaneously minimizing the residuals from the primary and the secondary.

For both of 2 steps, we used *Tiny Tim* to calculate $10\times$ over-sampled model PSFs based on the filters, the spectra (2M1207A: Bonnefoy et al. (2014), 2M1207 b: Patience et al. (2010)), the telescope’s actual focus, and the telescope jitter. We used the set of *Tiny Tim* parameters provided by Biretta (2014) to improve modeling the cold mask, diffraction spikes, and the coma. The focus parameters are interpolated to the precise time of the observations using the tabulated values provided by STScI⁵. To align the *Tiny Tim* PSF to the observed PSF of 2M1207 A, we moved the over-sampled PSF on a coordinate grid (grid size=0.001 pixel) using cubic interpolation, and searched for the position that minimizes the rms difference of the observed and the rebinned *Tiny Tim* PSF over a region centered on 2M1207 A with a 5-pixel-radius aperture centered on 2M1207 b excluded. Then we introduced another *Tiny Tim* PSF for 2M1207 b and fit the position of 2M1207 b and the scales of the *Tiny Tim* PSFs of 2M1207 A and b simultaneously by minimizing the residual from both primary and secondary. In the first step, we discovered that the difference of observed PSFs and model PSFs were very stable for a specified telescope roll angle and dithering position. Therefore, at the end of the first step, we derive 8 (2 roll angles \times 4 dithering positions) correction maps for each filter:

$$\text{Corr} = \text{Median}(\text{PSF}_{\text{obs.}} - \text{PSF}_{\text{model}}) \quad (1)$$

where $\text{PSF}_{\text{model}}$ was a combination of two scaled *Tiny Tim* PSFs for 2M1207 A and b. In the second round, we combined the correction map linearly with the two *Tiny Tim* PSFs to generate hybrid PSFs, and scaled the correction map together with the two PSFs so that the residual which is expressed as

$$\text{residual} = \text{Image} - a \cdot \text{PSF}_A - b \cdot \text{PSF}_b - c \cdot \text{Corr} \quad (2)$$

is minimized by least square fitting. We found that by introducing the correction term, the reduced χ^2 was decreased from ~ 10 to ~ 1 . Relative photometry was acquired from the scaling parameters of the *Tiny Tim* PSFs.

Our final step was to correct for a slight apparent trend between the position of the targets on the detector and their flux. We attributed this to a combination of slight changes in the PSF profile due to pixelation and to the effect of imperfectly corrected pixel-to-pixel sensitivity variations. We corrected for these apparent position-dependent flux changes by normalizing each photometric point by the median of all fluxes measured when the target was at the same position, i.e. combining data over 6 orbits. We note that this correction is small and, as we demonstrate in the next sections, cannot introduce arti-

cial modulations that resemble the long-period variations we identify in 2M1207b.

As our study is the first to present high-contrast, high-cadence observations, we provide a detailed analysis of the uncertainties and their impact on our results.

3.2. Uncertainty Analysis: White noise

First we estimated the photon noise for the photometry of 2M1207 b. The total photon noise of the photometry was calculated by combining the photon noise of every pixel, which was derived from count rates and detector gain. The photon noises in F125W and F160W are 1.33% and 1.02%, respectively.

Since the PSFs for the 2M1207 A and b were fitted simultaneously, the uncertainties for photometry and position of the primary and secondary were coupled. Errors in position measurements of 2M1207 A could potentially affect the photometry of 2M1207 b. We used a Monte Carlo (MC) method to evaluate the overall systematic of the PSF fitting. We applied photometry to images that were added with random Poisson noise and repeated the photometry procedure for 1000 times. The uncertainties for F125W and F160W photometry were found to be 1.34% and 1.12%, respectively.

3.3. Uncertainty Analysis: Flat field uncertainties

A further contribution to photometric uncertainties may be introduced by imperfectly corrected pixel-to-pixel sensitivity differences. 2M1207 b were observed at 8 different positions on the detector (2 rolls \times 4 dithering positions). Imperfect flat field correction could introduce position-dependent differences in the count rates. The uncertainty of WFC3 IR flat field is typically $\sim 1\%$ (Dressel 2012).

In PSF photometry, however, multiple pixels are fitted simultaneously, so that we expect the photometry to be less affected by high spatial frequency flat field noise, and have a lower than 1% uncertainty from the flat field errors. To verify this, we multiplied every image by an artificial flat field error mask (AFEM) – a uniformly distributed Gaussian noise array with mean of 1 and sigma of 1% – and repeated the PSF photometry on the resulting images. The analysis of these experiments resulted in almost identical light curve to the original, verifying that the flat field errors did not affect our photometry significantly (Figure 2, bottom panel).

4. VERIFICATION OF PHOTOMETRIC MODULATIONS AND AMPLITUDE ESTIMATE

4.1. Tests and Verification

The light curves that resulted from our photometry showed apparently sinusoidal modulations, discussed in more details in §.5. To verify that these modulations are intrinsic to the object and not results of our data reduction procedures or due to instrumental changes, we carried out three different tests.

First, we fitted sinusoids independently to the light curves of two filters to verify the similarity of the signal in the two bands (Figure 2, top panel). Inconsistent periods or light curve shapes would argue against a genuine signal. We found that the periods of the best fit sine waves were similar, $10.5^{+1.2}_{-1.3}$ h for F125W and $9.1^{+1.1}_{-1.0}$ h

⁵ <http://www.stsci.edu/hst/observatory/focus/FocusModel>

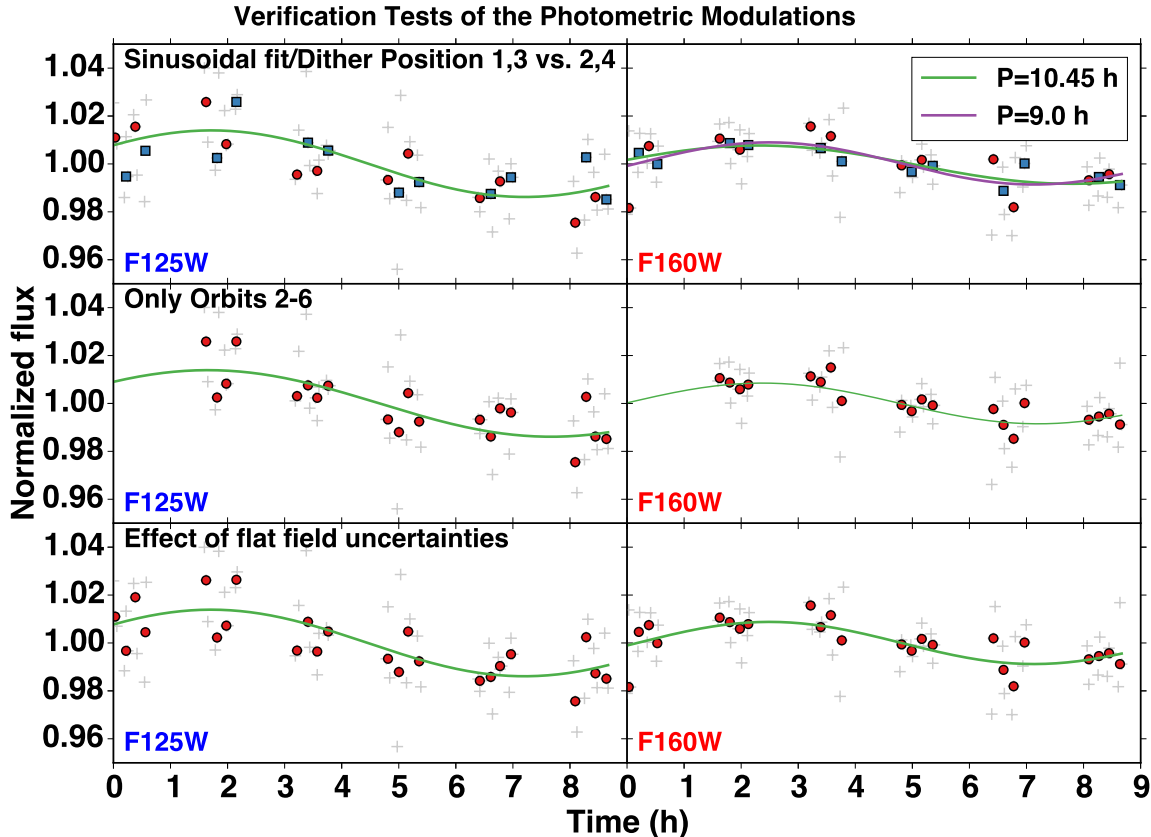


FIG. 2.— F125W (left) and F160W (right) light curves under different variability verification tests. Individual measurements are plotted with gray crosses. Photometric measurements of the same exposure sequence are binned, and binned photometry are plotted with points or squares. Best fitted sinusoidal curves are plotted with solid lines. *Upper*: binned measurements taken in dithering position 1 and 3 (red points) and that taken in 2 and 4 (blue squares) are plotted with different symbols. They demonstrate same trend of modulation. In upper left panel, green line is sinusoidal wave fitted with all parameter set free, and purple line is sinusoidal wave fitted with period set the same as that of F125W. *Middle*: sinusoidal waves fitted without using the data taken in Orbit #1. These curves are almost identical to the curves plotted in upper panel. *Lower*: photometry measured with AFEM-added images and best fitted sinul curves. These points and curves are also almost identical to those plotted in the upper panel.

for F160W. These periods are consistent within the uncertainty. Furthermore, these periods are not close to any timescales over which HST or WFC3 changes, and are very different from all timescales present in our observations (dithering timescales, integration times, and orbital timescales).

As a second test, we repeated the analysis neglecting the first orbit. The motivation behind this test is that, due to spacecraft thermal settling, the first orbits of HST observations are often slightly unstable, and neglected in high-precision studies (e.g. Mandell et al. 2013). Indeed, in our analysis 2M1207 A is significantly fainter in the first orbit (Figure 3) than in the subsequent ones. Our analysis based on orbits 2–6 found essentially identical results to our analysis using the whole 6 orbits, based on which we conclude that the first less reliable orbit does not affect our results significantly (Figure 2, middle panel).

As a third test, we explored whether a subset of images, perhaps due to imperfectly normalized or correlated with specific instrument states, could drive the light curves into an apparently sinusoidal shape. To test this possibility, we split the data into two temporally overlapping halves: subset one were images taken at dithering position 1 and 3, and subset two were those taken at dither-

ing position 2 and 4. For both subsets, we repeated our analysis independently. For both of F125W and F160W, two halves demonstrated similar sinusoidal modulations. Our analysis detect sinusoidal modulations in *both* subsets and in *both* filters, with periods and amplitudes consistent with those derived from the complete data set (Figure 2, upper panel).

These tests demonstrate that the modulation seen in our data are consistently present in the different filters, in the different time segments of the data, and in data obtained in different dithering positions. All of the three tests support the signal to be intrinsic to the target.

4.2. Amplitude and Period Measurements

We used a MC method to analyze the light curve, and provided amplitudes and periods as well as their uncertainties for both filters. We generated series of Gaussian distributed random noise with standard deviation same as the photon noise, add the noise to the original light curves, and fit sinusoids to the newly combined light curves. We repeated these procedures for 100,000 times and obtain the distributions of period and amplitude (Figure 4).

5. RESULT

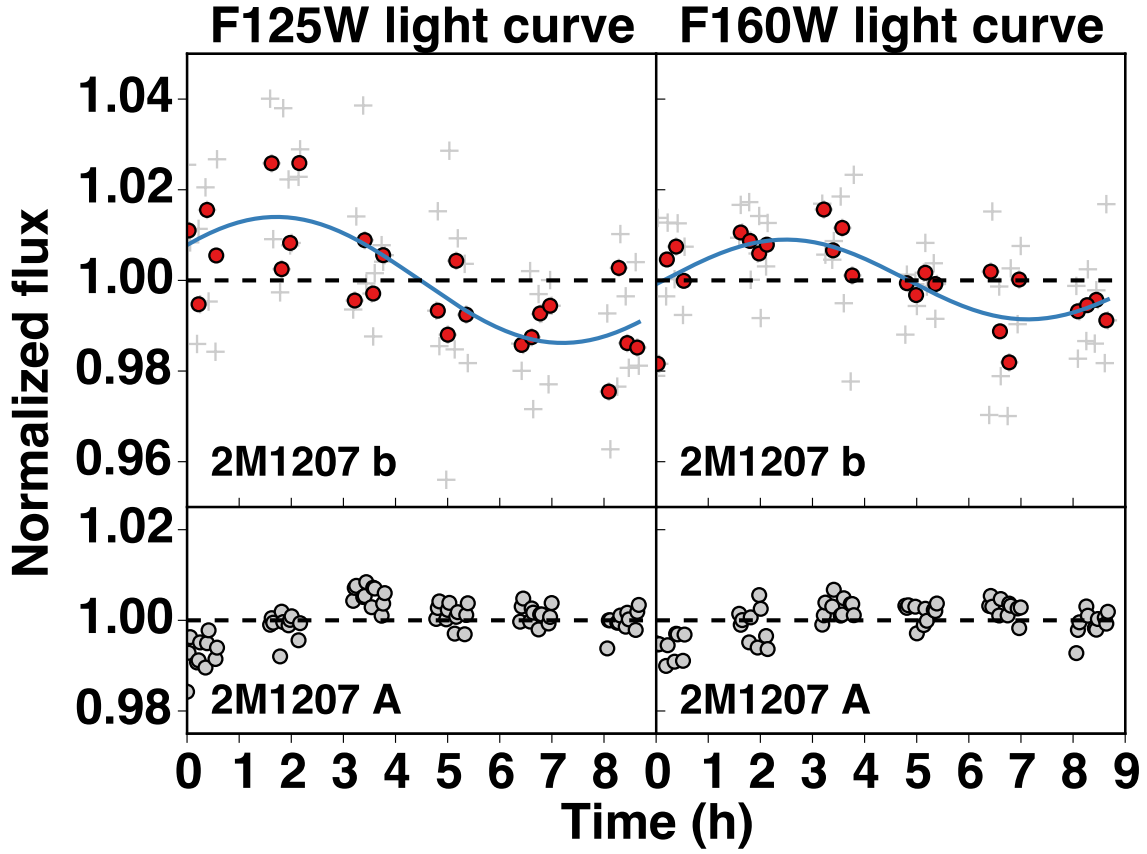


FIG. 3.— Normalized light curves for 2M1207 B (upper) and A (lower) with filter F125W (left) and F160W (right). Individual photometric measurement are plotted in gray crosses and binned photometry are plotted with red points. Best fitted sinusoidal waves are plotted with blue solid lines.

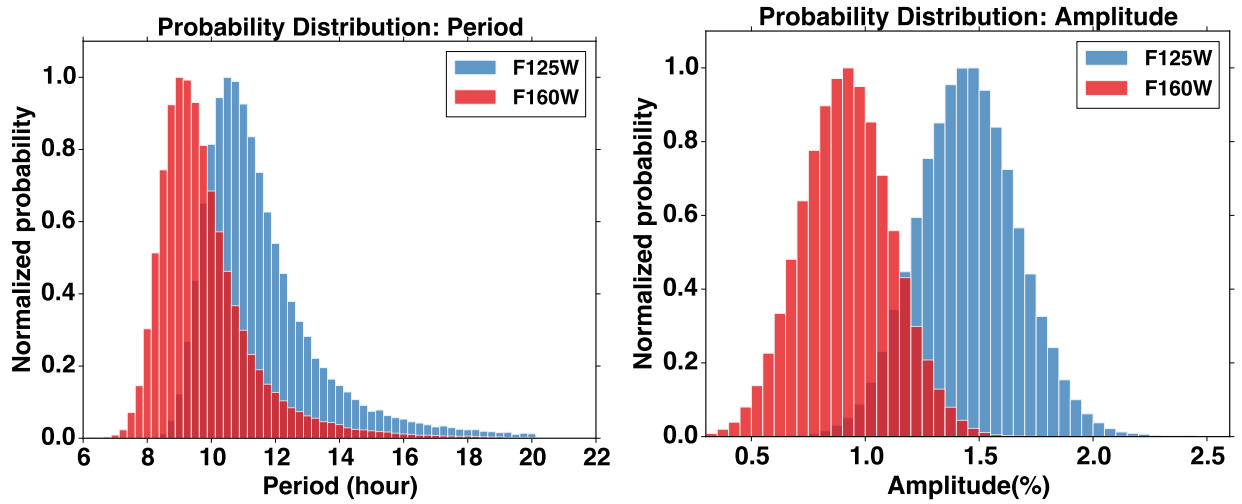


FIG. 4.— Distributions for periods (left) and amplitudes(right) for the light curve of F125W and F160W. The bin size for histograms of period is 0.25 hour and for that of amplitude is 0.5%. Histograms are normalized to the maximum. In the right panel, Gaussian profiles are fitted to the histograms of periods and plotted in solid lines.

We present the first high-resolution, high-cadence, and high-precision photometry of a directly imaged planet or planetary-mass companion. Our observations reveal a modulation in the light curve of the $\sim 4M_{\text{Jup}}$ companion 2M1207 b, the first detection of modulations in directly imaged planetary-mass objects. The best fit periods for F125W and F160W are $10.5^{+1.3}_{-1.2}$ and $9.1^{+1.1}_{-1.0}$ hour, respectively. We also fit the two band light curves together forcing the periods of two sinusoids to be the same, and obtained a period of $10.2^{+0.9}_{-0.8}$. The amplitudes for the normalized light curves are 1.45% and 0.92% for F125W and F160W, respectively.

We obtained high signal to noise photometry for both 2M1207 A and B (Figure 3). On average, the photometric contrast is 6.52 ± 0.01 mag for F125W and 5.77 ± 0.01 mag for F160W.

We found that the amplitudes in the two bands are significantly different. By fitting Gaussians to the MC fit result distributions, we determined that the amplitude for F125W is 1.45% with a standard deviation of 0.22%, and the amplitude for F160W is 0.92% with a standard deviation of 0.20%. The amplitudes of two bands are separated by more than 2σ . The amplitude for F125W is 1.58 times of that for F160W light curve.

6. DISCUSSION

An important result of our study is the direct measurement of the rotation period of a directly imaged planetary-mass object. In the left panel of Figure 5 we compare the rotation period of 2M1207 b to the solar system planets, β Pic b the only other directly imaged planet with an estimated period and measured $v \sin i$, and field brown dwarfs from the study of (Metchev et al. 2015). (Snellen et al. 2014) measured $v \sin i$ for β Pic b and demonstrated that it fits a trend defined by Solar System planets in which more massive planets have faster rotation rates. The interesting finding that β Pic b, an exoplanet that formed in a protoplanetary disk, follows this trend suggests a possibly connection between planet mass, initial angular momentum, and formation in a disk.

Excitingly, our measurement of the rotation period of 2M1207 b, a planet mass companion that has similar age to β Pic b, has a rotation period that fits in the same trend, as well as majority of brown dwarfs. As 2M1207 b and β Pic b evolve and cool down, they are expected to shrink to the size of Jupiter. Order of magnitude estimation based on the conservation of angular momentum results in final rotation periods of ~ 5 h and ~ 3 h (Snellen et al. 2014) for 2M1207 b and β Pic b, respectively, which still fit to the period vs. mass trend. Although 2M1207 A is known to host a circumsubstellar disk (Sterzik et al. 2004), the low mass of typical brown dwarf disks (Klein et al. 2003; Mohanty et al. 2013, e.g.) and its large separation argue against the possibility that 2M1207b has formed in a protoplanetary disk. The result that objects formed in different scenarios share the same trend of period vs. mass suggests that rotation periods – in absence of well-determined ages – may contribute insufficient evidence for a formation in a disk vs. in a cloud core environment. Although rotation rates may have limited value for deciphering formation pathways, measurements of mass, age, and rotation periods will map the angular momentum evolution of planetary-

mass objects and may place powerful constraints on the evolution of the internal structures of these contracting objects.

Our inferred rotation period is very similar to those of Jupiter and Saturn, which have periods of 9.9 and 10.5 hours, respectively. Moreover, our inferred rotation is sufficiently fast that—just as with Jupiter and Saturn—the atmospheric dynamics is likely to be rotationally dominated at regional to global scales (Showman & Kaspi 2013). The importance of rotation can be characterized by the Rossby number $Ro = U/\Omega L$, where U is the characteristic wind speed, Ω is the angular rotation rate ($1.7 \times 10^{-4} \text{ s}^{-1}$ for a 10-hour rotation period), and L is the characteristic horizontal length scale. Although the wind speeds are unknown, Showman & Kaspi (2013) presented a theory of the atmospheric circulation on brown dwarfs and directly imaged giant planets, which predicts wind speeds in the range of tens to hundreds of ms^{-1} depending on parameters. Global simulations of the atmospheric circulation using a one-layer model by Zhang & Showman (2014) predict a similar range. Considering wind speeds ranging from 10 to 1000 ms^{-1} , a circulation that is global in scale ($L = \text{Jupiter radius}$) implies Rossby numbers of 0.001 to 0.1 on 2M1207b (see Figure 1 in Showman & Kaspi (2013)). For a circulation whose length scale is 0.1 Jupiter radii, the Rossby numbers would range from 0.01 to 1 depending on wind speed. Thus, over almost the full range of plausible parameters, we expect that the large-scale circulation on 2M1207b—like Jupiter, Saturn, and most brown dwarfs—exhibits a Rossby number much less than one. This implies that the atmospheric circulation is rotationally dominated and that the horizontal force balance is approximately geostrophic, that is, a balance between Coriolis and pressure-gradient forces.

From the perspective of atmospheric dynamics, 2M1207b exhibits other important similarities to brown dwarfs. Its high effective temperature indicates that—like most brown dwarfs—2M1207b exhibit a strong interior heat flux presumably transported by convection, and that, by comparison, the external irradiation is negligible to the circulation. These similarities suggests that the overall dynamical mechanisms for driving an atmospheric circulation on 2M1207b should be similar to those on brown dwarfs. Thus, given the prevalence of IR light curve variability observed on brown dwarfs, it is unsurprising to find such variability on directly imaged planets like 2M1207b. Nevertheless, directly imaged planets generally have lower gravity than field brown dwarfs, and this will affect the details of the atmospheric circulation, potentially including the cloud patchiness. Further observations of 2M1207b and other directly imaged planets will help to elucidate these differences. Key questions for the future will include assessing the extent to which the atmospheric circulation on 2M1207b—including the existence of absence of zonal (east-west) jet streams, vortices, storms, and turbulence, and their effect on cloud patchiness—are similar or different than that on typical field brown dwarfs.

Furthermore, our observations allow us to compare the relative amplitudes in the J- and H-bands with the handful of brown dwarfs for which high-quality near-infrared time-resolved observations have been obtained. In the

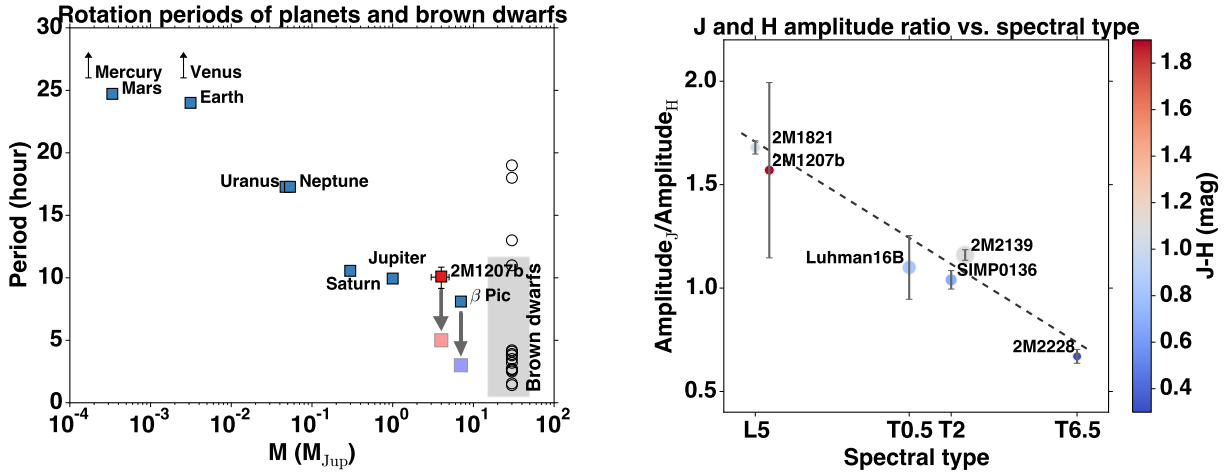


FIG. 5.— comparison of 2M1207’s rotation period and color change with brown dwarfs, β Pic b, and solar system planets. *Left*: period vs. mass plot for 2M1207 b (red square), solar system planets and β Pic b (blue squares), and brown dwarfs (black circles, gray shade). Final rotation rates for 2M1207 b and β Pic b estimated by conservation of angular momentum are plotted with faint red and blue squares, respectively. The mass of brown dwarfs are assumed to be $30 M_{\text{Jup}}$. The gray rectangle that has a $\pm 15 M_{\text{Jup}}$ range in x , and a $\pm \sigma$ of brown dwarf periods range in y , indicates a region where brown dwarfs most likely to appear in this diagram. Rotation period monotonically decreases with the increase of mass. *Right*: ratio of modulation amplitude in J and H band vs. spectral type for 2M1207 b and brown dwarfs. The point for 2M1207 b is shifted to $+x$ for half spectral type for clarification. The colors of the points represent J–H magnitude, and the sizes of the points are proportional to the J-band modulation amplitudes. The gray dashed line is the result of a linear fit to these points. Tight correlation of J- and H-band modulation amplitude ratio and spectral type is shown.

right panel of Figure 5, we compare the relative amplitude of J- and H-bands of 2M1207 b and brown dwarfs (Apai et al. 2013; Buenzli et al. 2012, 2015; Burgasser et al. 2013; Radigan et al. 2012; Yang et al. 2014) that have different spectral types and J–H colors.

We also find an interesting possible correlation between the spectral types of the objects and their J- to H-band amplitude ratios. In the right panel of Figure 5, we show that earlier spectral type objects have larger amplitudes at shorter wavelength than at longer wavelengths. Interestingly, although the J–H color of 2M1207 b is significantly redder, its relative amplitude ratio is very similar to that of 2M1821, which also has an L5 spectral type Yang et al. (2014). This exciting, but tentative trend must be confirmed on a larger sample of source that also sample a broader range of surface gravities as well as spectral types. If the larger sample verifies the trend suggested by our small sample, the amplitude ratio will provide a powerful probe of the spectral type and surface gravity dependence of vertical cloud structure.

7. CONCLUSIONS

In summary, from our J- and H-band high precision, high-cadence light curves we discovered sinusoidal modulations in the planetary-mass object 2M1207 b. This is the first detection of rotational modulations in a directly imaged planetary-mass object. The period is $10.2^{+0.9}_{-0.8}$,

similar to that derived from $v \sin i$ measurements for the directly imaged exoplanet β Pic b and significantly longer than most field brown dwarfs with known rotation periods. The amplitude ratio of J and H band is very similar to that of a field brown dwarf with identical L5 spectral type, although they have very different J–H colors.

Finally, we note that the observations presented here open an exciting new window on directly imaged exoplanets and planetary-mass companions. Our study demonstrates a successful application of high-cadence, high-precision, high-contrast photometry with planetary mass companion. We also show that these observations can be carried out simultaneously at multiple wavelengths, allowing us to probe multiple pressure levels. With observation of a larger sample and at multiple wavelengths, we will be able to explore the detailed structures of atmospheres of directly imaged exoplanets, and identify the key parameters that determine these.

Support for program number 13418 was provided by NASA through a grant from the Space Telescope Science Institute, which is operated by the Association of Universities for Research in Astronomy, Inc., under NASA contract NAS5-26555. The results reported herein benefitted from collaborations and/or information exchange within NASA’s Nexus for Exoplanet System Science (NExSS) research coordination network sponsored by NASA’s Science Mission Directorate. M.S.M. acknowledges support from the NASA Astrophysics Theory Program.

REFERENCES

- Ackerman, A. S. & Marley, M. S. 2001, *ApJ*, 556, 872
 Allard, F., Homeier, D., & Freytag, B. 2012, *Royal Society of London Philosophical Transactions Series A*, 370, 2765
 Apai, D., Radigan, J., Buenzli, E., Burrows, A., Reid, I. N., & Jayawardhana, R. 2013, *ApJ*, 768, 121
 Baraffe, I., Chabrier, G., Barman, T. S., Allard, F., & Hauschildt, P. H. 2003, *A&A*, 402, 701
 Barman, T. S., Macintosh, B., Konopacky, Q. M., & Marois, C. 2011, *ApJ*, 735, L39
 Berta, Z. K., Charbonneau, D., Désert, J.-M., et al. 2012, *ApJ*, 747, 35
 Biretta, J. 2014, *Space Telescope WFC Instrument Science Report*, 1, 10
 Bonnefoy, M., Chauvin, G., Lagrange, A.-M., Rojo, P., Allard, F., Pinte, C., Dumas, C., & Homeier, D. 2014, *A&A*, 562, A127
 Buenzli, E., Apai, D., Morley, C. V., Flateau, D., Showman, A. P., Burrows, A., Marley, M. S., Lewis, N. K., & Reid, I. N. 2012, *ApJ*, 760, L31

- Buenzli, E., Saumon, D., Marley, M. S., Apai, D., Radigan, J., Bedin, L. R., Reid, I. N., & Morley, C. V. 2015, *ApJ*, 798, 127
- Burgasser, A. J., Sheppard, S. S., & Luhman, K. L. 2013, *ApJ*, 772, 129
- Burrows, A., Sudarsky, D., & Hubeny, I. 2006, *ApJ*, 640, 1063
- Chauvin, G., Lagrange, A.-M., Dumas, C., Zuckerman, B., Mouillet, D., Song, I., Beuzit, J.-L., & Lowrance, P. 2004, *A&A*, 425, L29
- . 2005, *A&A*, 438, L25
- Currie, T., Burrows, A., Itoh, Y., Matsumura, S., Fukagawa, M., Apai, D., Madhusudhan, N., Hinz, P. M., Rodigas, T. J., Kasper, M., Pyo, T.-S., & Ogino, S. 2011, *ApJ*, 729, 128
- Dressel, L. 2012, *Wide Field Camera 3, HST Instrument Handbook*, 1
- Ducourant, C., Teixeira, R., Chauvin, G., Daigne, G., Le Campion, J.-F., Song, I., & Zuckerman, B. 2008, *A&A*, 477, L1
- Heinze, A. N., Metchev, S., & Kellogg, K. 2015, *ApJ*, 801, 104
- Helling, C., Ackerman, A., Allard, F., Dehn, M., Hauschildt, P., Homeier, D., Lodders, K., Marley, M., Rietmeijer, F., Tsuji, T., & Woitke, P. 2008, *MNRAS*, 391, 1854
- Klein, R., Apai, D., Pascucci, I., Henning, T., & Waters, L. B. F. M. 2003, *ApJ*, 593, L57
- Kostov, V. & Apai, D. 2013, *ApJ*, 762, 47
- Kreidberg, L., Bean, J. L., Désert, J.-M., et al. 2014, *Nature*, 505, 69
- Krist, J. 1995, in *Astronomical Data Analysis Software and Systems IV*, Vol. 77, 349
- MacKenty, J. W., Kimble, R. A., O’Connell, R. W., & Townsend, J. A. 2008, in *Society of Photo-Optical Instrumentation Engineers (SPIE) Conference Series*, Vol. 7010, Society of Photo-Optical Instrumentation Engineers (SPIE) Conference Series, 1
- Madhusudhan, N., Burrows, A., & Currie, T. 2011, *ApJ*, 737, 34
- Mandell, A. M., Haynes, K., Sinukoff, E., et al. 2013, *ApJ*, 779, 128
- Marley, M. S., Saumon, D., Cushing, M., Ackerman, A. S., Fortney, J. J., & Freedman, R. 2012, *ApJ*, 754, 135
- Marley, M. S., Saumon, D., & Goldblatt, C. 2010, *ApJ*, 723, L117
- Marois, C., Macintosh, B., Barman, T., Zuckerman, B., Song, I., Patience, J., Lafrenière, D., & Doyon, R. 2008, *Science*, 322, 1348
- Metchev, S. A., Heinze, A., Apai, D., Flateau, D., Radigan, J., Burgasser, A., Marley, M. S., Artigau, E., Plavchan, P., & Goldman, B. 2015, *ApJ*, 799, 154
- Mohanty, S., Greaves, J., Mortlock, D., Pascucci, I., Scholz, A., Thompson, M., Apai, D., Lodato, G., &Looper, D. 2013, *ApJ*, 773, 168
- Mohanty, S., Jayawardhana, R., Huelamo, N., & Mamajek, E. 2007, *ApJ*, 657, 1064
- Patience, J., King, R. R., De Rosa, R. J., & Marois, C. 2010, *A&A*, 517, A76
- Radigan, J., Jayawardhana, R., Lafrenière, D., Artigau, E., Marley, M., & Saumon, D. 2012, *ApJ*, 750, 105
- Showman, A. P. & Kaspi, Y. 2013, *ApJ*, 776, 85
- Skemer, A. J., Close, L. M., Szűcs, L., Apai, D., Pascucci, I., & Biller, B. A. 2011, *ApJ*, 732, 107
- Skemer, A. J., Hinz, P. M., Esposito, S., Burrows, A., et al. 2012, *ApJ*, 753, 14
- Snellen, I. A. G., Brandl, B. R., de Kok, R. J., Brogi, M., Birkby, J., & Schwarz, H. 2014, *Nature*, 509, 63
- Song, I., Schneider, G., Zuckerman, B., Farihi, J., Becklin, E. E., Bessell, M. S., Lowrance, P., & Macintosh, B. A. 2006, *ApJ*, 652, 724
- Sterzik, M. F., Pascucci, I., Apai, D., van der Blik, N., & Dullemond, C. P. 2004, *A&A*, 427, 245
- Yang, H., Apai, D., Marley, M. S., Saumon, D., Morley, C. V., Buenzli, E., Artigau, E., Radigan, J., Metchev, S., Burgasser, A. J., Mohanty, S., Lowrance, P. J., Showman, A. P., Karalidi, T., Flateau, D., & Heinze, A. N. 2014, *ApJ*, 798, L13
- Zhang, X. & Showman, A. P. 2014, *ApJ*, 788, L6